

Polarization in π^-p elastic scattering at 1180, 1250, and 1360 MeV/c*

E. Barrelet,[†] O. Chamberlain, W. Gorn, S. Shannon, G. Shapiro, and H. Steiner

Lawrence Berkeley Laboratory, University of California, Berkeley, California 94720

(Received 3 December 1976)

We have measured the polarization parameter in π^-p elastic scattering at laboratory momenta of 1180, 1250, and 1360 MeV/c in the angular interval $65^\circ < \theta_{\text{c.m.}} < 115^\circ$. The results were used to show that the polarized target used in these (and other similar) experiments was uniformly polarized. These measurements were also used to resolve pre-existing experimental discrepancies in the determination of the polarization parameter, and to clarify the behavior of scattering amplitudes in this energy range. We show that local measurements of this type are important in resolving discrete ambiguities affecting the energy continuation of the amplitudes. An important by-product of this experiment is the development of a fast method of reconstructing particle trajectories and fitting the elastic events, which could have a significant impact for future high-statistics experiments.

I. INTRODUCTION

We present here the results of a polarized-target experiment performed at the Bevatron as an adjunct to measurements of the polarization parameter for the reaction $\pi^-p \rightarrow \pi^0n$ which have already been published.¹ The objective of this auxiliary experiment was to study polarization in elastic scattering, with an experimental setup as close as possible to one used for the charge-exchange reaction, in a way which would allow us to calibrate the LBL polarized target. Schematically this can be done by using the analyzing power of the π^-p elastic scattering to compute the polarization of the target as a function of the relevant parameters, which is just the contrary of an ordinary measurement of a polarization parameter. This effort is justified because it provides us with a check of the various assumptions customarily made when using polarized targets, like target homogeneity.

As a by-product of this experiment, we obtained some precise values of the polarization parameter of π^-p elastic scattering, accumulated at 1180, 1250, and 1360 MeV/c in the central region of the center-of-mass scattering angle, between 65° and 115° . There is a particular interest in getting better data in this region, where the polarization parameter is peaked towards -1 . The method of zeros² allows one to make quantitative use of such local measurements and to correlate directly these regions of high polarization with the discrete ambiguities of the amplitude analysis.

Finally, in this paper we would like to put a particular emphasis on the presentation of our method of data analysis. This method, which goes far beyond the needs of this limited experiment, should be directly applicable to the next generation of measurements of differential cross section and polarization parameter.

II. THE EXPERIMENT

The experimental layout is shown in Fig. 1. The beam and the polarized target were essentially the same as have been used in the charge-exchange experiment of Shannon *et al.*^{1,3} The beam with a typical momentum bite of $\pm 1.5\%$ was positioned inside the target by an upstream steering magnet. It was electronically defined by a coincidence between different counters. The beam particles were measured by two hodoscopes. The one upstream yielded both x and y coordinates with a $\frac{1}{2}$ -in. resolution, while the downstream one yielded x only, with $\frac{1}{8}$ -in. resolution. The beam cross section inside the target was 2.5×2.0 cm, and its angular divergence was 2.5° full cone angle. Its intensity was about 7×10^5 π^- per pulse with a contamination of μ^- less than 4%. The polarized proton target (primarily 1,2 propane-diol), with length along the beam of 7.5 cm and a cross-sectional area 2.5×2.5 cm, yielded an average polarization of 0.48 with an average fluctuation of ± 0.02 (rms). We also collected data from a "dummy" target (essentially graphite) at each momentum. The target polarization was reversed every 2–3 hours.

The scattered-pion trajectory was measured by two proportional wire chambers, π_1 and π_2 , each made of two orthogonal planes of wires x and y . The recoil proton was measured by two similar wire chambers P_1 and P_2 . The wires were spaced by 2 mm and connected in groups, yielding a resolution ranging according to the plane from 0.6 to 1.4 cm. The efficiencies of π_1 and π_2 (and similarly of P_1 and P_2) were monitored by a count of the coincidence between the two scintillators R_1 and R_2 (L_1 and L_2). We noticed some variation of the efficiency with time (due to the detection electronics) which was corrected for in the subsequent analysis.

The trigger required the detection of one beam

particle, a "fast output" (indicating a pulse in some channel) from each wire chamber, and no particle detected in the veto counters surrounding the target. A typical Bevatron pulse yielded 40 to 80 triggers, of which $\frac{3}{4}$ were good events ("good" means a single coordinate in each wire plane, thus eliminating the trigger due to spurious fast-output signals). One-fifth of these good events turned out to be elastic events.

III. THE ANALYSIS

A. General

Our experimental layout allows us to do a complete reconstruction of the elastic events and provides us with four constraints. This can be figured out easily. When the beam trajectory is known, each prong of an elastic event depends only on 3 parameters: the position z of the apex along the beam, the center-of-mass scattering angle $\theta_{c.m.}$, and the azimuthal angle ϕ . These three parameters are determined uniquely by the coordinates (x_1, y_1) and (x_2, y_2) of the two impacts of each secondary particle on the two corresponding wire chambers. Therefore our four constraints are: (1) an angle-angle constraint expressing the equality of the two values of $\theta_{c.m.}$, determined by the pion track and the proton track, (2) a coplanarity constraint relating the two determinations of ϕ , and (3) two geometrical constraints, expressing the fact that the three trajectories have a common apex (one constraint is lost by the lack of a y coordinate in the downstream hodoscope). It

is also possible to reject the events for which the reconstructed apex lies outside the target. We call that "the target pseudoconstraint."

The geometrical constraints, acting indirectly as a momentum analysis, allow us to separate the elastic and quasielastic events from the rest of the background. The angle-angle and coplanarity constraints differentiate the elastic events and the quasielastic ones ("quasielastic" scattering means scattering on a bound proton inside a carbon or oxygen nucleus of the target).

The information concerning each individual event is sufficient to allow us to envisage the use of a geometrical- and kinematical-fitting program like THRESH-GRIND to obtain good accuracy. However, we have accumulated in this limited experiment 10^6 events, and one might wish to measure hundreds of times more. Therefore we found it more economical to write a specific program, fully accurate but making good use of the characteristics of our experimental layout and of the elastic kinematics. We managed to reconstruct an elastic event with less than 150 operations (additions, multiplications, and a few divisions), using an *interpolation polynomial* each time we had to evaluate a function. The practical program, although not optimized, yields around 10^4 events per CDC-6600 second and is able to reconstruct the trajectory-defining angles with a precision of 10^{-2} degrees, which corresponded in our calculation to the use of cubic interpolation polynomials and matched the statistical errors. This is shown in Fig. 2, where the difference between the pion

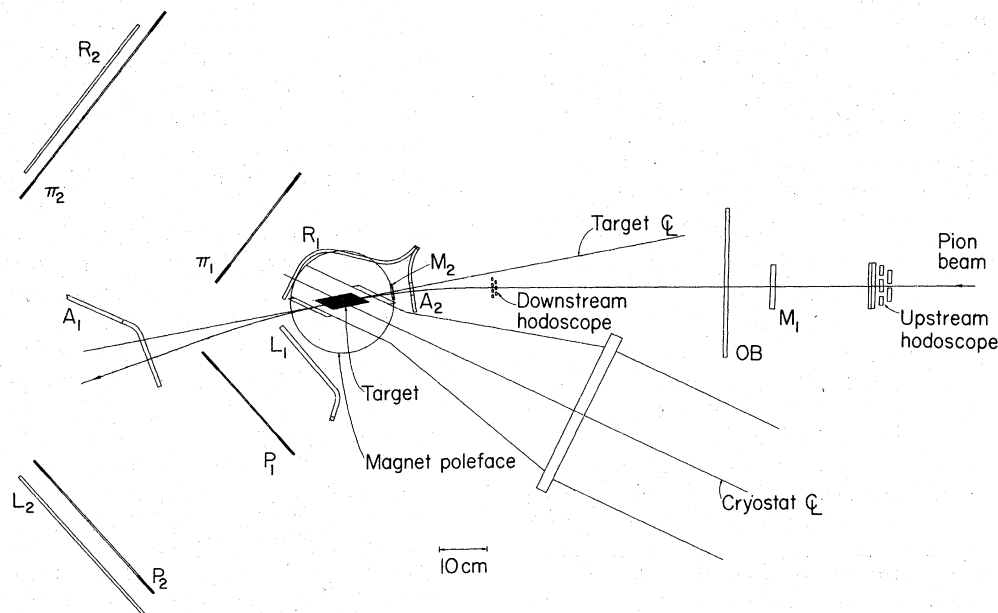


FIG. 1. Plan view of experimental arrangement showing the polarized target and the detectors. π_1 , π_2 , P_1 , and P_2 are multiwire proportional chambers; all other detectors are scintillation counters.

scattering angle in the laboratory frame, as measured from the pion track $\theta_\pi(\pi)$ itself, and that predicted from measurement of the recoil-proton track $\theta_\pi(p)$ is plotted as a function of the scattering angle θ_π . The quoted error is obtained by dividing the $\approx 1^\circ$ angular resolution for one event by the square root of the number of events ($\approx 10^4$). In the present case, the fact that $\theta_\pi(\pi) = \theta_\pi(p)$ is so well verified means that we have been able to fix the respective position of our detectors to ± 0.15 mm. This example shows that an important by-product of accuracy is the ability to trace the systematic errors associated with such experiments.

B. A practical algorithm

Prior to any programming, we had to write down explicitly *all* the algebra and statistics leading from the raw data to the polarization parameter, in the canonical algebraic form already mentioned (relying on interpolation polynomials). This involved the development of the special computing techniques described in the following section. What came out is a chain sequence of programs based on computing efficiency:

(1) First one computes a given set of trajectories through the magnet and the detectors, deduces from them the constraints entering into the geometrical-fit and kinematical-fit formulas, and uses them to construct tables of coefficients to be used by the next program.

(2) The second program reads the magnetic tapes containing the coordinates (wire numbers, hodoscope channels) for each event, performs the geometrical and kinematical fits, prepares the vital statistics such as monitor counts, average polarization, etc., and stores the event in the different histograms which are used later in the determination of the polarization parameter. Usually no more than 40 operations are necessary to decide that an event is inelastic and to dispose of it,

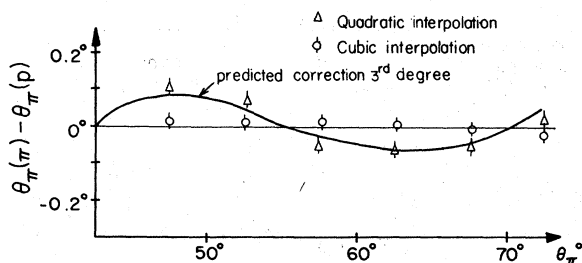


FIG. 2. The difference between the pion scattering angle in the laboratory frame, measured from the pion track only $\theta_\pi(\pi)$, and that predicted from measurement of the recoil-proton track $\theta_\pi(p)$, is plotted as a function of the scattering angle θ_π .

whereas, to treat an elastic event, one needs 150 operations, few compared to the input-related operations.

(3) The third step, relying on hand calculations and small programs, consists in summing up the data from different runs, computing corrections, choosing the binning, and computing the polarization parameter and its error.

A few data tapes have been processed several times by the second program in order to improve by iteration the determination of the parameters defining the geometry of the experimental apparatus, which are fed into the first program. The bulk of the data tapes have been processed only once, yielding definitive results.

C. Special computing techniques

These techniques, detailed in Ref. 4, give an elegant solution to the two arduous parts of the calculation of an elastic event.

1. *The reconstruction of an outgoing particle in a magnetic field decreasing continuously with the distance from the center of the target.* To solve the general problem requires three nonalgebraic equations where the three track-defining parameters z , θ , and ϕ are the unknowns. But we introduced three simplified formulas which yield our unknowns with a precision of about 1%:

$$\begin{aligned}\theta_{c.m.} &= A_1(x_1, x_2), \\ z &= A_2(x_1, \theta_{c.m.}), \\ \phi &= A_3(y_2 - y_1, \theta_{c.m.}, z),\end{aligned}\quad (1)$$

where A_1 , A_2 , and A_3 are simple rational expressions and (x_1, y_1) and (x_2, y_2) are the intercepts with the two wire chambers. We also computed the first-order corrections to these formulas in order to reach the 10^{-2} -degree precision shown in Fig. 2. A higher precision is easy to obtain mathematically but has no physical meaning with our apparatus. There is a simple geometrical representation of (1), which has much predictive power. If we consider (Fig. 3) the different elastic events corresponding to the same scattering angle

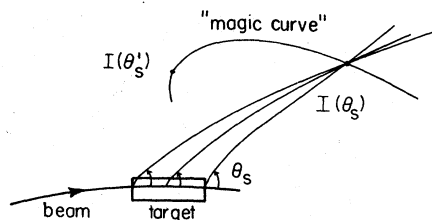


FIG. 3. The reconstruction of elastic events uses the fact that all the trajectories corresponding to the same scattering angle θ_s almost intersect at the same point I , whose locus is the "magic curve."

θ_s , the different pion (or proton) trajectories, projected on the xOz plane of symmetry, intersect almost at the same point $I(\theta_s)$. When we vary θ_s (i.e., $\theta_{c.m.}$) and the momentum of the scattered particles accordingly, $I(\theta_s)$ generates a curve that we call the "magic curve." Conversely, knowing the straight line determined by (x_1, x_2) and a linear approximation of the magic curve, one can find their intersection I and compute with an empirical polynomial the corresponding value of θ_s (or $\theta_{c.m.}$). Some refinements of this picture, shown in Ref. 4, allow us to visualize the first-order corrections to (1).

2. *The best-fit procedure.* Used in general programs like GRIND or SQUAW, this procedure has been revised to simplify the algebra, and also to be applicable to our experiment where error distributions are not Gaussian. Our main simplification consists in introducing new variables which allow us to subdivide our system of eleven equations with four constraints (described above in Sec. III A) into four independent subsystems. For example, if we choose as our new variables $\theta_\pi(\pi)$ and $\theta_\pi(p)$, defined in Fig. 2, we get a subsystem of two equations, according to (1): $\theta_\pi(\pi) = A_1(x_{\pi_1}, x_{\pi_2})$, $\theta_\pi(p) = A_1(x_{p_1}, x_{p_2})$. For each wire-chamber coordinate x taking discrete values, the point $M [\theta_\pi(\pi), \theta_\pi(p)]$ will have discrete positions in the plane of Fig. 4. The acceptance of the four x detectors defining the point M is a sort of truncated pyramid centered on M , which is the product of the trapezoidal distributions of each coordinate. Any elastic event should yield, instead of the "measured" point M , a "true" point T lying on the first bisector (angle-angle constraint) and

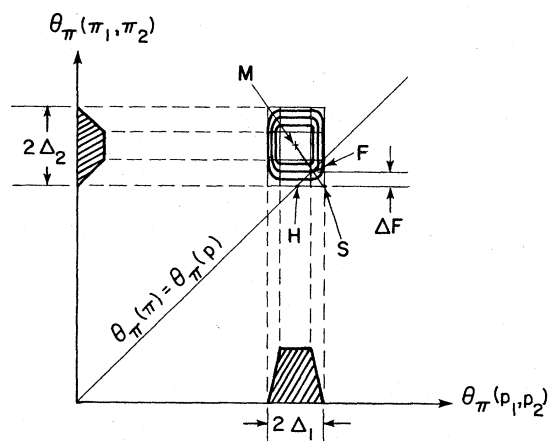


FIG. 4. On this angle-angle plot (variable as in Fig. 2) the point M representing the two measurements of the scattering angle and their trapezoidal error distributions yield a 3-dimensional truncated pyramid whose base is a rectangle centered on M . The fitted point F is on the first bisector (angle-angle constraint).

within the rectangle limiting the "accepted" points. The fitted point F , defined as the expected value of T , is situated almost on the diagonal MS of the rectangle. Knowing the components Δ_1 and $-\Delta_2$ of MS given by interpolation polynomials in the variable θ_π , we have computed it. The fitted value θ_π^F of θ_π is defined by any coordinate of F , and the maximum fitted error $\delta\theta_\pi^F$ is the maximum component of FS . We have also computed the variable $X_{\text{angle-angle}} = MF/MS$, which is histogrammed in Fig. 5 and agrees nicely with a solid curve predicted by using only the known shape of the pyramid of Fig. 4. A nice feature of this χ distribution, compared to a Gaussian one, is its edge at $\chi = \pm 1$, which allows us to verify that there is no unknown contribution to our experimental errors and to define a "pure background" by the condition $|\chi| > 1$. For each of our four constraints there is a χ variable with a distribution similar to that of Fig. 5.

IV. THE POLARIZATION PARAMETER

A. The calibration of the experiment

1. The polarized target

The first objective of our experiment was to study the effects of the inhomogeneity and the fluctuations of the polarization of protons inside the target. The answer was that such effects were accurately measured by our method and that they did not significantly bias our results. The method, detailed in Ref. 4, consists of computing the average asymmetry yielded by elastic πp scattering integrated over a large range of center-of-mass scattering angle around 90° . This quantity (≈ -0.75) is fixed by the property of strong interactions. Its apparent variations will reflect the variations of the target polarization. Firstly we have drawn a 3-dimensional map of the polarization inside the target, with a 1-cm resolution. It turned out to be uniform within the statistical error which varied from 2% at the center of the target, where the beam flux was maximum, to 7% at the periphery. It is also possible to discard global effects, such as a difference between the center of the target and its periphery, within a smaller error ($\approx 1\%$). If we suppose that the target inhomogeneity was the worst compatible with our data, the polarization parameter would be affected only on the edges of our angular range and by less than 3%. Secondly we have watched the variations of polarization with time. They are monitored by an NMR probe⁵ which is certainly reliable on a short time scale, owing to the proven uniformity of the target. Our analysis described in Ref. 4 has convinced us that the NMR monitor has not

drifted by more than 1% throughout the experiment, while the absolute calibration of the target, involving the measurement of the thermal-equilibrium polarization signal, exhibited a 2.5% irreproducibility.

2. The detectors

The fluctuations in the detection efficiency were on the order of 10%, in some cases as high as 50%. This unwelcome effect has turned into an advantage because it forced us to develop a method which is not sensitive to these fluctuations. It consists of selecting the background events which are predominantly (90%) quasielastic and are believed to yield no appreciable asymmetry. Therefore, for each of our 200 detectors, we expect to find the same ratio n^+/n^- of the total background counts for the runs with an upward target polarization to the downward ones. After detection and elimination of a few abnormal runs, we have shown that the fluctuation of the ratio n^+/n^- around its average η is purely statistical, except for two ailing wires which gave a 15-standard-deviation false asym-

metry and were treated separately. This result proves that by alternating upward and downward target polarization we have been able to average out the false asymmetries.

B. The calculation of the polarization parameter

1. Formulas

One can find in the literature different formulas relating the polarization parameter to the scattering data.⁶ The conclusion of our careful search, detailed in Ref. 4, favors the simplest of all formulas. Using the expression

$$n^i = M^i(I_0 + I_1 T^i) \quad \text{with } n^i = \langle N^i \rangle \quad (2)$$

we have computed, by multiple integration, the expected value n^i of the number of events N^i to be counted in a given angular bin during a certain period labeled i , during which the number of particles in the beam was M^i and the target polarization T^i . The asymmetry A defined as $A = I_1/I_0$ is roughly equal to the polarization parameter P . A detailed study of the multiple integration leading to (2) yields all the corrections to apply to A in order to get P . They are discussed later in Sec. IV B 3.

The study of Eq. (2) has convinced us to use the "simplified" estimators Y_0 and Y_1 of I_0 and I_1 , obtained by replacing, successively, the index i in (2) by + and -, as if there had been no fluctuation of the target polarization around its "up" and "down" mean values T^+ and T^- . The simplified estimators are not biased and are essentially as efficient as the χ^2 estimators. They are

$$Y_0 = \frac{T^+ N^- / M^- - T^- N^+ / M^+}{T^+ - T^-}$$

and

$$Y_1 = \frac{N^+ / M^+ - N^- / M^-}{T^+ - T^-}.$$

The errors on these quantities are Gaussian and easy to compute, yielding the σ^2 of the asymmetry distribution which simplifies, because we have $T^+ = -T^- = T$:

$$\sigma_A^2 = \frac{M^+ + M^-}{M^+ M^-} \frac{(1 + A\bar{T})(1 - A^2 T^2)}{4I_0 T^2}, \quad (4)$$

with

$$\bar{T} = T(M^+ - M^-)/(M^+ + M^-).$$

The simplicity of this formula resides in the fact that it is sufficient to make a separate count for the "up" runs and the "down" ones of the events (N^+) and of the beam particles (M^+), to compute the mean target polarizations (T^+), and then merge these numbers in formulas (3) and (4). Moreover

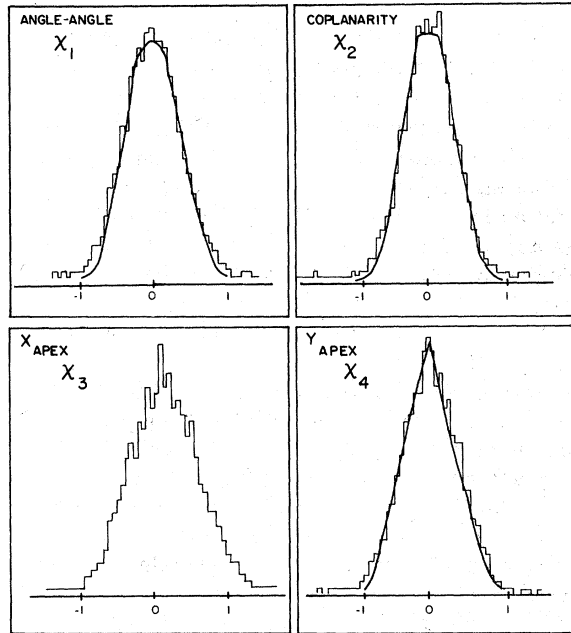


FIG. 5. Distributions (histograms) in the normalized deviations from constraints. Each χ is the deviation from perfect satisfaction of a constraint equation divided by the maximum deviation attributable to the finite channel sizes in the proportional wire chambers. The agreement between the solid curves, calculated purely on proportional chamber resolution, and the experimental histograms indicates that chamber resolution is a greater contributor than multiple scattering to the deviations from constraints.

the asymmetry and its error depend on the ratio $\eta' = M^*/M^-$. This ratio has to be corrected if the efficiency of every detector has varied during the experiment. Instead of doing this delicate correction (of the order of 2%), we point out that the parameter η , determined at the end of Sec. IV A 2, was automatically corrected because the number of background events is proportional, not to beam flux only, but to its product with the detector efficiency. Further analysis has shown that the error affecting it is purely statistical and small (0.2%), due to the substantial number of background events. This method could even be used to correct the false asymmetries generated by a variation of detector efficiencies.

2. Background evaluation

It is important to understand quantitatively the nature of the background in order to evaluate the proportion of background events inside our sample of elastic events, and also because the background is used as a monitor. We had three independent ways of studying the background.

First we can empirically subtract the elastic events from the total and observe the remainder. Practically, when interested in a given variable, we have drawn the two histograms of this variable corresponding to the two orientations of the target polarization. Then, for each couple of corresponding bins containing, respectively, N^+ and N^- events, we applied the two formulas (3). This generates two new histograms: the "added" one, with Y_0 events per bin, which simulates a target chemically identical but unpolarized, and the "subtracted" one, with Y_1 events per bin, simulating a pure hydrogen target. The comparison has shown us that, for the χ variables corresponding to the angle-angle and coplanarity constraints, the distribution of the background is almost flat below the elastic peak. For the 2 geometrical constraints it is almost as peaked as the elastic peak. Therefore, to obtain a good separation of hydrogen events, we have formed the new variable $\chi^2 = (\chi_{\text{angle-angle}})^2 + (\chi_{\text{coplanarity}})^2$. To this unconventional " χ^2 " we have assigned the same sign as $\chi_{\text{angle-angle}}$, yielding an elastic peak symmetric around 0. On Fig. 6(b) the "subtracted" χ^2 distribution exhibits the absence of hydrogen events for $|\chi^2| > 2$. This proves that there is no radiative or multiple-scattering tail to consider (at the level of 4×10^{-4}), and that the background below the hydrogen peak is not polarized.

Secondly we have repeated for the carbon "dummy"-target data the same analysis as for the normal target. Outside the elastic peak the carbon data reproduces well our background as we ex-

pected it (by this we mean that carbon and oxygen nuclei behave similarly and that there is no significant hydrogen inelastic reaction in our background). We could even detect a small hydrogen peak in the carbon data corresponding to a 0.05% contamination of our dummy target.

Thirdly we can reproduce surprisingly well all the characteristics of our background by a very simple model of quasielastic scattering; we have supposed that the bound protons have a Fermi momentum uniformly distributed in a sphere of 200 MeV/c radius. The effective number of bound protons is the real one divided by a screening factor of 2.6 (very close to $A^{1/3}$). The predictions of this model are simple to establish, since kinematics tells us that the χ coplanarity variable expresses a mapping of the transverse y component of the Fermi momentum, while the χ angle-angle variable maps a component of the Fermi momentum in the scattering plane. For example, the 200-MeV/c cutoff of the Fermi momentum yields a clear cutoff of the background for $|\chi_{\text{coplanarity}}| > 4$. Practically the model reproduces within 10% the χ^2 distribution of Fig. 6(a) up to $|\chi^2| = 25$.

We conclude from these 3 convergent analyses that our background is quasielastic scattering and that it is quantitatively predictable. However, we have been able to succeed in this analysis only because our precise reconstruction of the apex distribution, coupled with the subsequent use of the target pseudoconstraint, has allowed us to eliminate another type of background, twice more abundant, resulting from a forward quasielastic scattering with a π^- detected by the proton telescope and proton in the pion telescope.

3. The results

Table I presents the polarization parameters that we have obtained at 3 energies and 16 angles by the following procedure: First we have histogrammed the $\cos\theta_{c.m.}$ variable, within 0.05 intervals, independently for both orientations of the target. The "signal cut," defined by $|\chi^2| < 0.5$, selected 85% of the elastic events with a 5% contamination (up from 2% at the peak). Second we have applied Eqs. (3) and (4) to each angular bin in order to compute the asymmetry A and its error σ_A . Third we have computed the corrections transforming this rough asymmetry $A \pm \sigma_A$ into the real polarization parameter $P \pm \Delta P$. The biggest correction is the background subtraction. The background is totally absent from the numerator Y_1 of the asymmetry A [see Fig. 6(b)], while it exists for the denominator Y_0 and varies slowly with χ^2 [Fig. 6(a)]. The evaluation of this background is suggested by the results of Sec. IV B 2: The extra-

polarization of the χ^2 distribution of the background below the elastic peak is guided by what our Fermi-momentum model told us, plus the fact that the background is pure for $|\chi|^2 > 2$. Practically, we took a linear extrapolation of the background from $-4 < \chi^2 < -2$ and from $2 < \chi^2 < 4$, except for the two edges of our angular domain where the limited acceptance of our detectors acts as a cut in the χ^2 variable (one advantage of our definition of χ^2 is that, when positive χ^2 's are cut, we use only negative ones, and conversely). The effect of nonlinearity in the background distribution was smaller than the statistical error and neither affected the polarization parameter. We have remarked that the proportion of background does not depend appreciably on the scattering angle, and therefore we have computed a single correction factor for each energy. This fact is simply understood in terms of our model: The scattering angle and the differential cross section are almost the same for the free protons and the bound protons inside the signal cut, which corresponds to a fixed region of the Fermi-momentum space. Next we have taken into consideration the fact that the ap-

parent target polarization is the real one multiplied by $\cos\phi$, where ϕ is the angle between the magnetic field and the normal to the scattering plane. Therefore we have divided the asymmetry by the mean value of this $\cos\phi$ for all events falling in each angular bin, determined easily to be $\langle \cos\phi \rangle \approx 1 - \frac{1}{2}\langle \phi^2 \rangle$. This correction varies regularly with the scattering angle from 0.5% to 1.1%. The other corrections that we have considered were neglected, being smaller than 0.5%. The "binning" error, smaller than 0.2%, fell into this category, but in our opinion this type of error should not be included at this stage of the analysis. Let us recall that this correction is of the form

$$\left[\left(\frac{d\sigma}{d\omega} \right)'' / \left(\frac{d\sigma}{d\omega} \right) - \left(P \frac{d\sigma}{d\omega} \right)'' / \left(P \frac{d\sigma}{d\omega} \right) \right] \frac{\Delta^2}{2}. \quad (5)$$

Therefore it can always be computed, when one knows the rms width Δ of each angular bin, by fitting the differential cross section and polarization data in order to evaluate their second derivatives appearing in the formula. But if we consider how different the local curvatures obtained from the same data by different fitting methods are, we

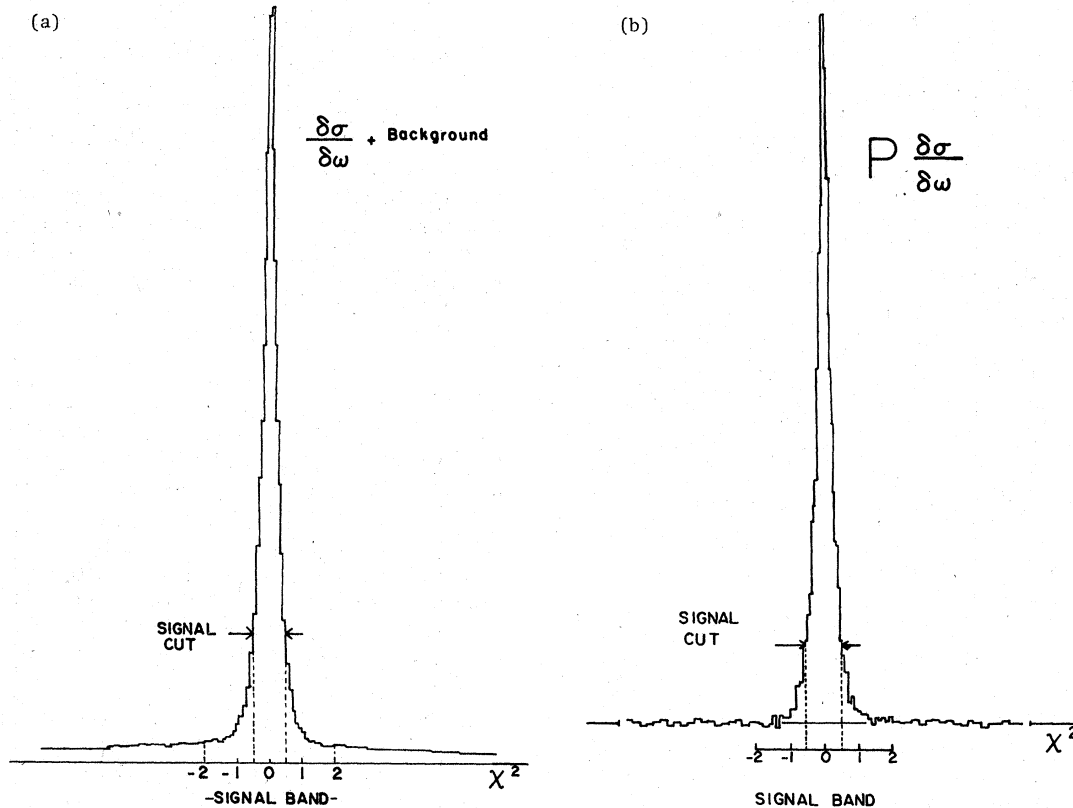


FIG. 6. The χ^2 variable combines the angle-angle and the coplanarity constraints to achieve the best separation of elastic events. Instead of the two χ^2 distributions corresponding to the two orientations of the target polarization (see Sec. IV B 2), we show the "added" distribution in (a) simulating an unpolarized target and the "subtracted" one in (b) simulating a pure hydrogen target. The cut $|\chi^2| > 2$ means pure background, while the signal cut $|\chi^2| < 0.5$ yields 85% of the elastic events with 5% background contamination.

feel that the correction would not be reproducible. The errors quoted in Table I are purely statistical. The normalization error, characteristic of the polarized target and its readout system, has been estimated to $\pm 6\%$. Our calibration of the target has suggested to us that the relative normalization error between two different energies is not greater than 1%. (In Sec. V we shall try to learn more about the normalization error by using the results of our amplitude analysis.) The cumulative effect of the other systematic errors has been estimated to be less than 1%, except for the points at $\cos\theta_{c.m.} = \pm 0.375$, where it is less than 3%. The angular resolution $\Delta(\cos\theta_{c.m.})$, defined as in (5), was ± 0.014 before the binning and became ± 0.02 after the binning. The biases affecting the measurement of $\cos\theta_{c.m.}$, as observed in Fig. 2, were around 3×10^{-4} , but they become of the order of 0.003 when one takes into consideration the uncertainty of the relative positions of the wire chambers and the beam.

V. AMBIGUITIES OF π^-p AMPLITUDE ANALYSES BETWEEN 1.0 AND 1.4 GeV/c

A. Conflicting data

A simple look at the compilation⁷ of π^-N data enables us to compare the new polarization data of Table I to older ones. A discrepancy appears between a first category of experiments (CERN-Holland,⁸ Hansroul,⁹ and ours), where the average polarization around $\cos\theta_{c.m.}=0$ is not far from $-1.$, and a second category (Cox¹⁰), where the absolute value of the polarization is noticeably smaller. Another more subtle effect concerns the shape of the polarization curve. Our data exhibit a broad minimum (or even two distinct minima) supposedly associated, as in the CERN-Holland⁸ data, with a sharp rise at $\cos\theta_{c.m.}=0.4$, while in some other data the minimum is narrower and rounder. The first of these two effects is very likely due to the difficulty of the absolute calibration of a polarized target, and the second to the different angular resolutions of the experiments.

B. The determination of the zeros

The purpose of the rest of this article is to use these local features of the data to study the discrete ambiguities of the amplitude analysis according to the method of zeros.² The principles of this method are illustrated by Fig. 7. For each scattering angle $\theta_{c.m.}$, the two classical parameters $d\sigma/d\omega$ and P are transformed into the two "transverse cross sections" $\Sigma^+ = (d\sigma/d\omega)(1+P)$ and $\Sigma^- = (d\sigma/d\omega)(1-P)$, which are equal to the square modulus of the two transversity amplitudes F^+

TABLE I. Polarization parameter $P(\cos\theta_{c.m.})$ in $\pi^-p \rightarrow \pi^-p$ scattering. The error is statistical only; the overall normalization error is $\pm 6\%$; the rms width of the $\cos\theta_{c.m.}$ bins is 0.02.

| $\cos\theta_{c.m.}$ | 1360 MeV/c | 1250 MeV/c | 1180 MeV/c |
|---------------------|--------------------|--------------------|--------------------|
| -0.375 | -0.260 ± 0.045 | -0.091 ± 0.058 | -0.046 ± 0.064 |
| -0.325 | -0.436 ± 0.033 | -0.324 ± 0.043 | -0.257 ± 0.052 |
| -0.275 | -0.603 ± 0.027 | -0.518 ± 0.038 | -0.436 ± 0.045 |
| -0.225 | -0.685 ± 0.026 | -0.531 ± 0.037 | -0.599 ± 0.041 |
| -0.175 | -0.769 ± 0.025 | -0.696 ± 0.035 | -0.744 ± 0.041 |
| -0.125 | -0.849 ± 0.025 | -0.761 ± 0.035 | -0.744 ± 0.040 |
| -0.075 | -0.863 ± 0.025 | -0.862 ± 0.034 | -0.823 ± 0.040 |
| -0.025 | -0.852 ± 0.026 | -0.917 ± 0.035 | -0.859 ± 0.045 |
| 0.025 | -0.825 ± 0.028 | -0.880 ± 0.035 | -0.908 ± 0.048 |
| 0.075 | -0.810 ± 0.028 | -0.882 ± 0.036 | -0.921 ± 0.045 |
| 0.125 | -0.816 ± 0.030 | -0.943 ± 0.036 | -0.894 ± 0.042 |
| 0.175 | -0.753 ± 0.032 | -0.893 ± 0.039 | -0.891 ± 0.044 |
| 0.225 | -0.731 ± 0.035 | -0.955 ± 0.041 | -0.902 ± 0.047 |
| 0.275 | -0.677 ± 0.040 | -0.828 ± 0.047 | -0.822 ± 0.052 |
| 0.325 | -0.706 ± 0.050 | -0.825 ± 0.053 | -0.726 ± 0.058 |
| 0.375 | -0.685 ± 0.071 | -0.669 ± 0.072 | -0.664 ± 0.074 |

and F^- .

In the vicinity of a complex zero of a transversity amplitude, one can write

$$F^\pm = A(\cos\theta - a - ib), \quad (6a)$$

$$\Sigma^\pm = |F^\pm|^2 = |A|^2[(\cos\theta - a)^2 + b^2]. \quad (6b)$$

Therefore the existence of a zero explains the parabolic shape of Σ^\pm near $\cos\theta = a$, as seen in Fig. 7 for Σ^- near $\cos\theta = 0.4$. On the same figure one can see the four other zeros of the F^+ and F^- amplitudes, although the shapes of the Σ^+ and Σ^- curves are complicated by the mutual influence of these zeros. The second zero of Σ^- yields a

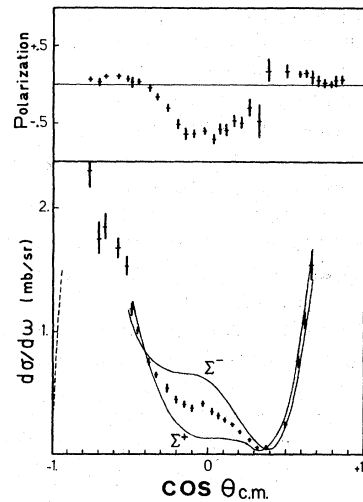


FIG. 7. Example of π^-p elastic-cross-section and polarization data taken from Albrow *et al.* (Ref. 8). The solid lines indicate the transversity cross section $\Sigma^+ = d\sigma/d\omega \times (1+P)$.

secondary minimum near $\cos\theta = -0.15$. A third and a fourth zero are seen in Σ^+ near $\cos\theta = +0.35$ and -0.05 , and a fifth one produces the backward dip¹¹ at $\cos\theta = -1$. We have determined these five zeros by fitting directly different data of the πN compilation,⁷ for beam momenta varying between 0.8 and 2.0 GeV/c, with a program¹² designed specially for that purpose. This program proceeds in two steps.

Firstly, we express $d\sigma/d\omega$ and $P d\sigma/d\omega$ as a sum of orthogonal functions. Rather than using Legendre functions, which are orthogonal when uniformly weighted in the interval -1 to 1 , we use functions that are constructed to be orthogonal with the weight factor determined from the points at which there are data and the errors on those data. The program then uses this orthogonality property to evaluate the coefficients of the polynomials in our sum (the method of moments).

Secondly, the program expresses the transverse cross section $\Sigma^*(\theta)$ in terms of the variable $e^{i\theta}$. Since powers of $e^{-i\theta}$ are implicitly involved it is expedient to multiply Σ^* by $e^{iN\theta}$, where N is the upper limit of the polynomial-expansion sum, before seeking its polynomial expansion. The roots (zeros) of this polynomial are then computed. Σ^- is also represented because $\Sigma^-(\theta) = \Sigma^*(-\theta)$.

Among the roots yielded by this method, we have seen a clear distinction between the "stable" ones,² which constitute an approximation of our zeros, and the "unstable" ones, distant from the physical region, which are artifacts. The only dubious case was associated with the appearance of a sixth zero with a large imaginary part above 1.5 GeV/c. The errors affecting this method are computed according to the prescriptions of Ref. 13. This means that we shall be concerned by the non-Gaussian character of the statistical distribution of the nearby zeros pointed out by Urban, but not by the mathematical error resulting from the truncation of the expansion of $\Sigma^*(\theta)$, which affects only the distant zeros. Conventionally the position of each zero in the $e^{i\theta}$ plane is transformed into the complex $\cos\theta$ plane and then into the complex Mandelstam variable t . By repeating the analysis independently at different energies, i.e., different values of the Mandelstam variable s , we obtain a collection of points representing the zeros in the 3-dimensional space $(s, \text{Re}t, \text{Im}t)$. It is easy to connect these points in order to produce the trajectories followed by the zeros when the energy is varied (see Fig. 8). The zeros of Σ^+ (dots) and those of Σ^- (circles) must be treated separately, except for the values of $\cos\theta$ around ± 1 where they become confused. They have been determined mainly from CERN-Holland data⁸ and ours because of the experimental discrepancies mentioned

earlier. However, because of the lack of data between $s = 3.5$ and $s = 4.1$ GeV², we have used data from other experiments in their "amalgamated" form, obtained as described in Ref. 14. The advantage of this amalgamation method, besides the fact that it used the world's data, is that it yields a smooth energy dependence (it fits implicitly segments of the zero trajectories). We have treated separately the backward region ($\cos\theta < -0.9$), for which we had good differential cross sections¹¹ but no polarization data. Around 1 GeV/c there is a backward dip which can be parameterized locally in the following form: $d\sigma/d\omega = A(\cos\theta - z_0)$, with $z_0 = -1 - \epsilon$. Providing ϵ is small, it can be shown that fitting the value of z_0 localizes the corresponding zero z of the transverse cross section in the $\cos\theta$ plane through the relation

$$|z + 1| = \epsilon \quad (7)$$

Equation (7) tells us that the backward zero F is at a given small distance ϵ from the backward edge of the physical region or, equivalently, that the projection of F on the $(s, \text{Re}t)$ plane of Fig. 8(a) is situated on a segment centered on this edge (see the triangles). This shows that the F trajectory is entering the physical region around $s = 3.0$ GeV, almost tangentially to its edge.

C. Study of the trajectories of zeros

1. The real parts

Figure 8(a) suggests a very simple empirical pattern for the projection of the zero trajectories on the real Mandelstam plane $(\text{Re}s, \text{Re}t)$: They never cross each other and therefore their energy continuation is unambiguous. However, there is a slight contradiction between our zeros and those which have been reconstructed¹⁵ from the recent Saclay phase shifts¹⁶: Contrary to ours, the two central zero trajectories B' and D' [see dotted lines on Fig. 8(a)] cross each other for $s = 3.1$ GeV/c². This corresponds to 1180 MeV/c, the first momentum for which we have measured the polarization parameter. Our data, like CERN-Holland's, are not compatible with a trajectory crossing at this energy. Qualitatively, two zeros with the same abscissa in the complex $\cos\theta$ plane yield a single minimum of the Σ^* curve instead of two distinct ones (see Fig. 7) and therefore a single narrow peak of the polarization parameter instead of the broad peak of Table I. In order to solve by continuity the ambiguities of the amplitude analysis at all energies, it is important to know whether these two zero trajectories cross each other or not. An error would affect the determination of the amplitude not only locally near $s = 3.1$ GeV², but also for all higher energies.

This means that a *local* measurement of $d\sigma/d\omega$ and P (for momenta around 1200 MeV/c and angles defined by $-0.4 < \cos\theta_{c.m.} < +0.5$), coupled with the fact that zeros are local parameters, may yield important information concerning the amplitude *globally*.

2. The imaginary parts

The imaginary parts of our zeros have an unknown sign [see Eq. (6b)]; therefore we have plotted only their absolute value in Fig. 8(b) (top). These are the well-known discrete ambiguities of the amplitude analysis that we shall not try to solve absolutely, but only relative to our lowest energy $s_0 = 2.5 \text{ GeV}^2$. We shall fix a positive sign for the imaginary part at $s = s_0$. If there is a "critical point" C , defined by $\text{Im}t = 0$, the trajectory crosses the physical region (see α in Fig. 9); otherwise $\text{Im}t$ stays positive as in the case of β . When the initial assignment of the sign of $\text{Im}t$ is wrong, the true trajectories α' or β' are the symmetric counterparts of α or β with respect to the

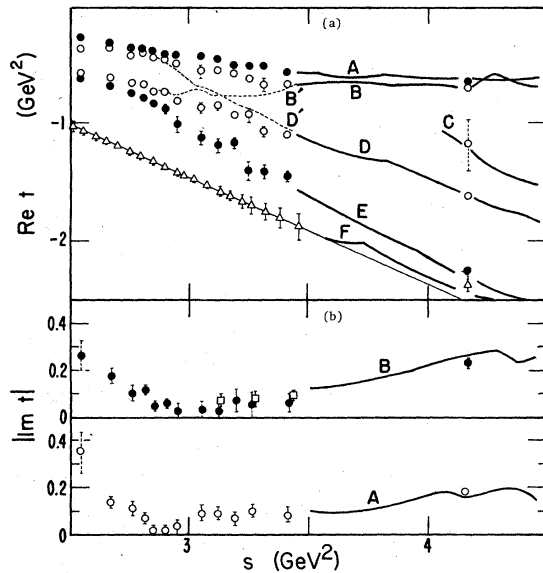


FIG. 8. The zeros of the π^+p transversity amplitudes F^+ and F^- , respectively, represented by dots \bullet and circles \circ , are projected on the two planes $(s, \text{Re}t)$ and $(s, |\text{Im}t|)$, where s and t are the conventional Mandelstam variables. They have been determined from CERN-Holland data alone first, then merged with our new data (squares \square), the error bars are computed by a method which works even in the non-Gaussian case. They are dashed when the local data are not reliable. A special analysis locates the backward zero (triangles \triangle). The six trajectories, A to F , generated by these zeros are indicated in the region where CERN-Holland data are lacking by a plain curve obtained from the other experiments via the "amalgamation" realized by the Carnegie-LBL group (Ref. 14).

real axis. It is crucial to determine the "critical points" along each trajectory. This can be done by using two criteria. Firstly, for each critical point there must be a minimum in the $|\text{Im}t|$ -versus- s curve for which $\text{Im}t = 0$. Secondly, this minimum must be a branch point where the slope changes its sign abruptly, instead of being a parabolic minimum where the slope becomes null gently. In the π^+p elastic scattering we have seen two possible critical points in the region between $s = 2.5$ and $s = 3.5 \text{ GeV}^2$, one on the A trajectory, one on the B trajectory, and none on the others. But our two criteria are not easy to apply due to the following experimental errors:

(1) The imaginary parts of zeros are very sensitive to the systematic errors mentioned in Sec. V A; the data of Ref. 10, characterized by a lower absolute value of the polarization than CERN-Holland's⁸ and ours, yield much larger imaginary parts of zeros. But even a realistic $\pm 8\%$ uncertainty in the target polarization transforms into a $\pm 30\%$ uncertainty in the imaginary part of the B trajectory at 1250 MeV/c.

(2) The simultaneous presence of two nearby "critical" zeros around $s = 3 \text{ GeV}^2$ and $\cos\theta = 0.4$ yields a very low differential cross section and a rapidly varying polarization, as seen in Fig. 7. Therefore these data are locally very sensitive to the background subtraction and to the binning errors, in a way which cannot be evaluated *in abstracto*.

(3) The statistical errors affecting the determination of zeros are not Gaussian, an effect predicted in Ref. 13 and seen in Fig. 10, which shows the distribution of the "A" zero obtained at 1055 MeV/c ($s = 2.9 \text{ GeV}^2$), when we give to the data some random fluctuations around their measured values compatible with the experimental errors. In practice we have computed such plots at different energies, and the error bars drawn in Figs. 8(a), 8(b) represent a 66% confidence interval (containing two-thirds of the projected points).

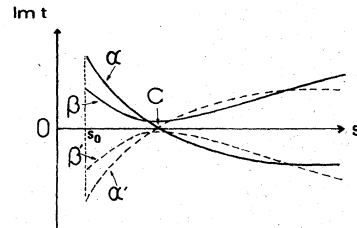


FIG. 9. Two cases, presented schematically, in which the projections of a zero trajectory on the $(s, |\text{Im}t|)$ plane have a minimum near zero, as A and B do in Fig. 8. In the case α (or α') there is a true critical point. The slope criterion can be used to distinguish between α and β , or between the corresponding cases α' and β' .

But we are not entitled to apply a χ^2 fit to such non-Gaussian points.

In spite of all these experimental uncertainties, we consider that the minimum observed for both A and B trajectories around $s = 3 \text{ GeV}^2$ in the $|\text{Im}t|$ -versus- s plot of Fig. 8(b) satisfies our first criterion of a critical point. Our second criterion cannot be fully applied because of insufficient data, although we do see an indication of a slope reversal for the A trajectory at $s = 2.9 \text{ GeV}^2$.

D. The absolute calibration of the polarizations

The critical points introduced previously provide us with an absolute calibration of the polarization parameter, because, at any points where the zero trajectories cross the physical region, the transverse cross section Σ^* (or Σ^-) is null, implying that the polarization parameter reaches an absolute minimum (or maximum) equal to -1 (or $+1$).

The same calibration points have been introduced differently in Ref. 17 as points where the ratio g' of the spin-flip amplitude g to the spin-nonflip amplitude f is equal to $\pm i$. The "inherent flaw" of the approach, as noted by the authors, is relying on a previous determination of f and g from the experimental data. Our study of critical

points tells us that this attitude is particularly dangerous because this is exactly the place where two different sets of amplitudes are perfectly ambiguous. This danger is hidden in an energy-dependent phase-shift analysis, while an energy-independent analysis has to choose clearly between the α -type and the β -type solution of Fig. 9. We have found previously an objective criterion which is not much affected by the uncertainty affecting the calibration of the polarization: An abrupt reversal of slope observed in the $|\text{Im}t|$ -versus- s plot is sufficient to establish the existence of a critical point. A large slope, as in the case of trajectory A compared to B , is favorable for detecting the effect.

A target, calibrated at a critical point, can be operated at various energies with a negligible drift of the calibration constant as seen in Sec. IV A 1. In the case of the π^+p elastic scattering, the assumption of the existence of a critical point on the A trajectory around $1050 \text{ MeV}/c$ should allow us to improve considerably the precision of the experimental data shown in Fig. 7, because it makes possible an absolute calibration of the target polarization. We would need ten polarization points, instead of two, for $\cos\theta$ between 0.3 and 0.5 in order to see the successive minimum and maximum of $P(\cos\theta)$, each of them with a precision of, let us say, ± 0.03 if we want an estimation of the calibration constant to $\pm 3\%$. This means, of course, using a much larger number of incoming pions than in previous experiments.

VI. CONCLUSION

We have measured the polarization parameter of elastic π^+p scattering in a region where two major previous experiments had yielded discrepant data. This fact was attributed to the errors affecting the calibration of the target. Our results support the higher absolute values of the polarization parameter. As the sources of systematic errors are the same for all experiments, we have envisaged an absolute calibration of the target based on the existence of critical points around $1050 \text{ MeV}/c$, where the polarization parameter equals 1. We have shown that this is feasible, although it requires a sophistication of the present experimental methods.

The importance of improving the quality of the polarization data has appeared to us when studying the discrete ambiguities affecting the energy continuation of the amplitudes. It is not yet possible to solve definitely the ambiguities associated with the existence of critical points near $1050 \text{ MeV}/c$. The ambiguity associated with a possible trajectory crossing at $1180 \text{ MeV}/c$ seems to be solved. Our solution is opposite to the one retained in a recent

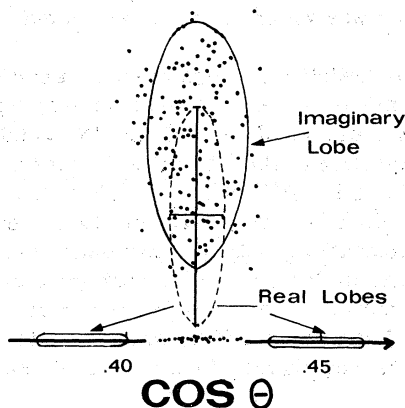


FIG. 10. The distribution of points observed here represents the statistical dispersion of the "A" zero within the complex $\cos\theta$ plane at $1055 \text{ MeV}/c$. If the usual linearization method was valid, this distribution would be the 2-dimensional Gaussian characterized by the 1-standard-deviation ellipse shown here (dashed line). On the contrary, the actual distribution is made of a pair of imaginary conjugated lobes (the lower one is not shown) corresponding to a pair of complex-conjugate zeros of the transverse cross section $\Sigma^-(\theta)$, and the real lobes generated by a pair of real zeros of Σ^- . In this second case the estimated position of the zero of the amplitude is taken to be the average of the two real zeros of Σ^- , which is distributed on the real axis between the two real lobes.

phase-shift analysis.¹⁶ From a more technical point of view, we have met the initial objective of the experiment concerning the determination of the distribution of polarization within the target (uniform to $\pm 7\%$) and the reliability of the polarization NMR monitor.

An important by-product of this analysis is the fast method for reconstructing particle trajectories and fitting the elastic events, which opens the way to future high-statistics experiments with a very low computing cost per event.

ACKNOWLEDGMENTS

We wish to express our thanks to Dr. John Jaros and Dr. Albert Bridgewater for their essential role during the data-acquisition phase of this work, and to Raymond Z. Fuzesy and Geoffrey O'Keefe, who contributed greatly to the construction and successful installation of the proportional chamber detectors. Our thanks also to Leonard Anderson, who participated in the initial analysis of this experiment, and to Marcel Urban for very helpful discussions about the data analysis.

*This research was done with support from the United States Energy Research and Development Administration.

†Present address: Laboratoire de Physique Nucléaire des Hautes Energies, École Polytechnique, Palaiseau, France.

¹S. R. Shannon, L. Anderson, A. Bridgewater, R. Chaffee, O. Chamberlain, O. Dahl, R. Fuzesy, W. Gorn, J. Jaros, R. Johnson, R. Kenney, J. Nelson, G. O'Keefe, W. Oliver, D. Pollard, M. Pripstein, P. Robrish, G. Shapiro, H. Steiner, and M. Wahlig, *Phys. Rev. Lett.* **33**, 237 (1974).

²E. Barrelet, thesis, Paris, 1970 (unpublished); and *Nuovo Cimento* **8A**, 331 (1972).

³S. R. Shannon, thesis, Lawrence Berkeley Laboratory Report No. LBL-2607, 1974 (unpublished).

⁴E. Barrelet, Lawrence Berkeley Laboratory Report No. LBL-4236, 1975 (unpublished).

⁵C. Morehouse, thesis, Lawrence Berkeley Laboratory Report No. UCRL-19897, 1970 (unpublished).

⁶See, for instance, P. R. Robrish, thesis, Lawrence Berkeley Laboratory Report No. LBL-1334, 1972 (unpublished), pp. 44-49.

⁷Particle Data Group, Lawrence Berkeley Laboratory Report No. LBL-63, 1973 (unpublished).

⁸M. G. Albrow, S. Andersson/Almehed, B. Bosnjaković, C. Daum, F. C. Ern , Y. Kimura, J. P. Lagnaux,

J. C. Sens, and F. Udo, *Nucl. Phys.* **B37**, 594 (1972).

⁹M. Hansroul, thesis, Lawrence Berkeley Laboratory Report No. UCRL-17263, 1967 (unpublished).

¹⁰C. R. Cox, P. J. Duke, K. S. Heard, R. E. Hill, W. R. Holley, D. P. Jones, F. C. Shoemaker, J. J. Thresher, J. B. Warren and J. C. Sleeman, *Phys. Rev.* **184**, 1453 (1969); also Rutherford High Energy Laboratory Report No. RHEL/M/137, 1968 (unpublished).

¹¹D. G. Crabb, R. Keller, J. P. O'Fallon, T. J. Richards, R. J. Ott, T. Trischuk, J. Va'vra, and L. S. Schroeder, *Phys. Rev. Lett.* **27**, 216 (1971); R. J. Ott, J. Trischuk, J. Va'vra, T. J. Richards, and L. S. Schroeder, *Phys. Lett.* **42B**, 133 (1972).

¹²E. Barrelet and M. G. Fouque, LPNHE École Polytechnique internal report, 1969 (unpublished).

¹³M. Urban, thesis, Paris, 1973 (unpublished).

¹⁴D. P. Hodgkinson, R. L. Kelly, R. E. Cutkosky, and J. C. Sandusky, Lawrence Berkeley Laboratory Report No. LBL-3048 (unpublished). The amalgamated data have been kindly communicated to us under a preliminary form by R. E. Cutkosky and R. Kelly.

¹⁵Private communication from Particle Data Group.

¹⁶R. Ayed and P. Bareyre (Saclay), paper presented at the Second International Conference on Elementary Particles, Aix-en-Provence, 1973 (unpublished).

¹⁷G. R. Plattner and A. D. Bacher, *Phys. Lett.* **36B**, 211 (1971).